

Imaginary phonon modes and phonon-mediated superconductivity in Y_2C_3 Niraj K. Nepal ¹, Paul C. Canfield,^{1,2} and Lin-Lin Wang ^{1,*}¹Ames National Laboratory, Ames, Iowa 50011, USA²Department of Physics and Astronomy, Iowa State University, Ames, Iowa 50011, USA

(Received 24 July 2023; revised 6 January 2024; accepted 30 January 2024; published 21 February 2024)

For Y_2C_3 with a superconducting critical temperature (T_c) ~ 18 K, zone-center imaginary optical phonon modes have been found for the high-symmetry $I-43d$ structure due to C dimer wobbling motion and electronic instability from a flat band near Fermi energy. After lattice distortion to the more stable lowest-symmetry $P1$ structure, these stabilized low-energy phonon modes with a mixed C and Y character carry a strong electron-phonon coupling to give rise to the observed sizable T_c . Our work shows that compounds with the calculated dynamical instability should not be simply excluded in the high-throughput search for new phonon-mediated superconductors. Moreover, we have studied the phase stability of the $I-43d$ structure by calculating the enthalpy of different structural motifs of binary compounds containing group-IV elements at the 2:3 composition and also exploring the energy landscapes via *ab initio* molecular dynamics near and out of the $I-43d$ structure. Our results show that the $I-43d$ -type structures with C dimers are preferred in the low to medium pressure range. Because of the wobbling motion of the C dimers, there are many local energy minimums with degenerated energies. Thus, the ensemble average of many $I-43d$ -distorted structures with C dimer wobbling motion at finite temperature still gives an overall $I-43d$ structure.

DOI: [10.1103/PhysRevB.109.054518](https://doi.org/10.1103/PhysRevB.109.054518)**I. INTRODUCTION**

The computational search for new phonon-mediated superconducting (SC) compounds has become an active field since the discovery of the SC critical temperature (T_c) near room temperature for metal hydrides under high pressure (~ 200 GPa) [1–6]. The search requires the computation of electron-phonon coupling (EPC) matrices within the density functional perturbation theory (DFPT) [7,8] to estimate T_c using Migdal-Eliashberg approximations [9–13]. However, compounds with calculated imaginary phonon modes are regarded as dynamically unstable and often discarded as promising candidates in high throughput [6]. As the phonon eigenmodes are solved in the quasiharmonic approximation, if some diagonal elements of the dynamical matrix are negative, the square root will give imaginary values for frequency, which correspond to the local maximum instead of minimum for the potential energy surface. It means the total energy of the system can be lowered via distortion by following the eigenvectors of these imaginary phonon modes, for which the frequencies are usually plotted as negative values. On the other hand, some well-known SC are metastable, such as YPd_2B_2C [14,15]. In this study, using yttrium sesquicarbide (Y_2C_3) as an example among rare-earth carbides R_2C_3 (R = rare earth, Y and La) with their SC being discovered and improved over the years [16–21], we find that the high-symmetry body-centered-cubic (bcc) Pu_2C_3 -type structure, Pearson symbol $cI40$ in space group $I-43d$ (220), is dynamically unstable with zone-center imaginary optical phonon

modes, which, once stabilized, carry a large EPC strength (λ) to give the sizable T_c . Thus, overlooking new compounds with the similar imaginary phonon modes in high-throughput search can leave out promising SC candidates.

Y_2C_3 in the space group $I-43d$ (220) with C dimers was first synthesized in 1969 using high-pressure, high-temperature techniques [16] to show T_c ranging from a low of 6 K to a high of 11.5 K [16]. Subsequent experiments with thorium (Th) alloying increased the T_c to 17 K in $(Y_{0.7}Th_{0.3})_2C_3$ [22]. Recently, in 2004, for the samples prepared under 4.0–5.5 GPa followed by different heat treatment and sintering conditions, a T_c up to 18 K in binary Y_2C_3 has been observed [17]. Electronic structure calculations have found that the states near the Fermi energy (E_F) are hybridized [23–25] between Y $4d$ and C-C antibonding $2p$ orbitals with an interesting flat band [23,25] close to the E_F , as well as highly degenerated Kramers-Weyl points at ~ 1 eV below the E_F [26]. It has been proposed that the sensitivity of SC properties for the related La_2C_3 [27] with respect to the synthesis condition is due to the change of density of states (DOS) at the E_F from C deficiency [24,25]. An earlier EPC calculation [25,28] on Y_2C_3 has focused only on two zone-center modes; a Y-dominated mode at 175 cm^{-1} (5.2 THz) and the C-C bond stretching mode at 1442 cm^{-1} (43.3 THz), and found a much larger EPC contribution from the Y-dominated than C-C bond stretching mode. However, here with the DFPT calculation over all the phonon modes, we find that the high-symmetry $I-43d$ structure is dynamically unstable with zone-center imaginary phonon modes of C dimer wobbling motion due to electronic instability from the flat band along the Γ - N direction at E_F . By following the lattice distortion of the imaginary modes with full relaxation, more stable

*llw@ameslab.gov

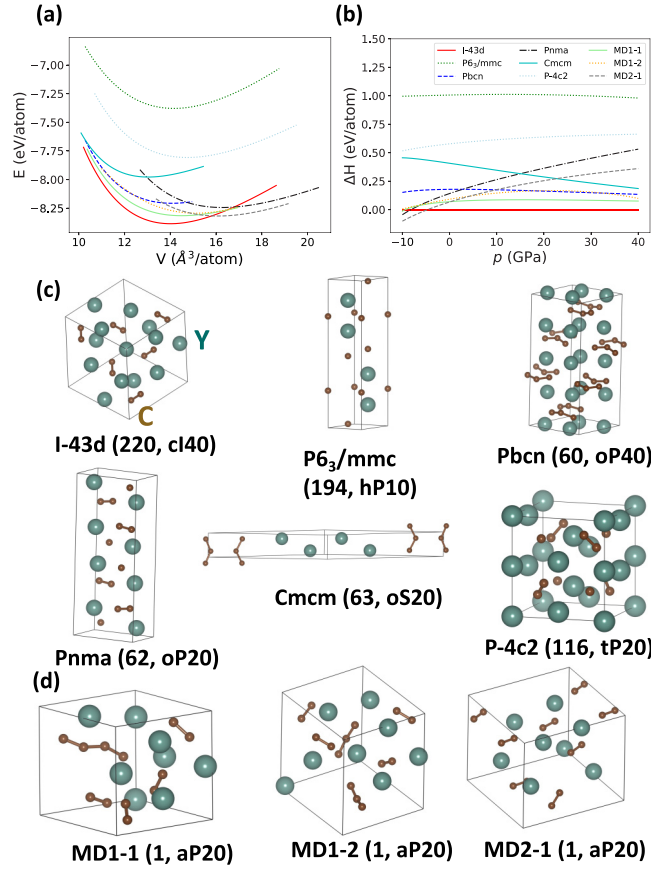


FIG. 1. (a) Energy (E) vs volume (V) plots for Y_2C_3 in the various structural motifs of the binary compounds containing group-IV elements at the composition of 2:3 and the structures close to the I -43d phase obtained from *ab initio* molecular dynamics (MD) simulations. (b) Enthalpy difference (ΔH) calculated for each phase vs pressure (p) with respect to the I -43d phase. (c) Fully relaxed Y_2C_3 in the different structural motifs as plotted in (a) and (b). (d) Fully relaxed Y_2C_3 structures obtained from the MD simulations under pressure of 20 GPa (MD1-1 and MD1-2) and -5 GPa (MD2-1). The space-group number and Pearson symbol are also shown in parentheses.

low-symmetry structures of Y_2C_3 have been found, where the imaginary modes become stabilized in a low-energy range, i.e., lower than the Y-dominated modes. These stabilized low-energy phonon modes carry large λ , which contributes significantly to T_c . The imaginary phonon modes can also be stabilized with a large electronic smearing and under pressure, with the latter enhancing the T_c in a trend, agreeing with the previous experiment [17].

II. COMPUTATIONAL DETAILS

We used the QUANTUM ESPRESSO (QE) package [29,30] with ultrasoft pseudopotentials [31,32] for ground-state and EPC calculations. The exchange-correlation energy was approximated by the Perdew-Burke-Ernzerhof (PBE) functional [33]. The kinetic energy cutoff of 50 Ry, Brillouin zone (BZ) sampling of $(6 \times 6 \times 6)$ \mathbf{k} -point mesh, and a Gaussian smearing of 0.05 eV were utilized for the ground-state

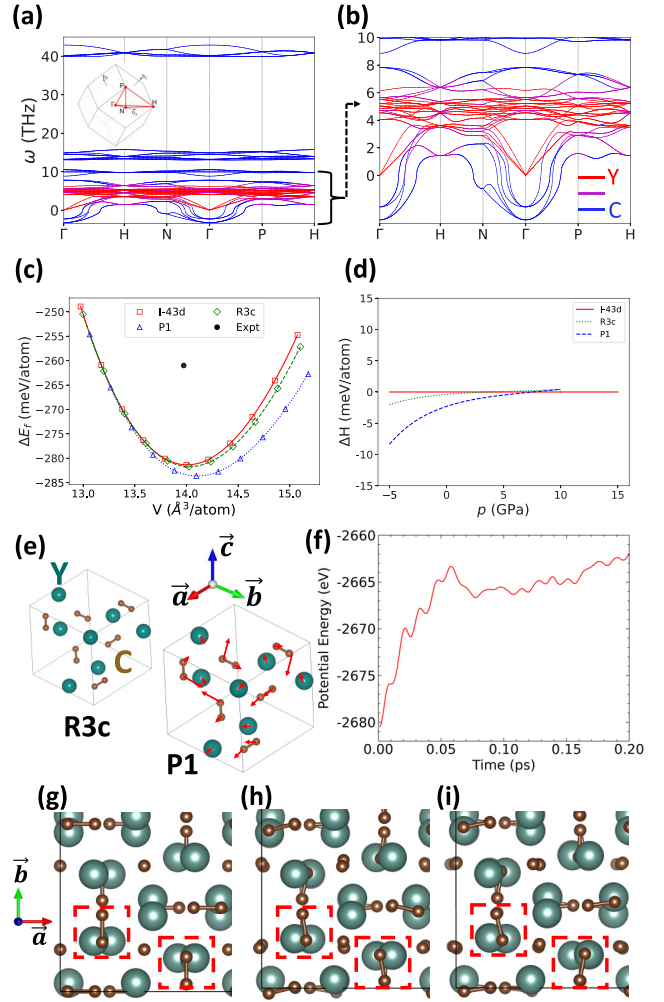


FIG. 2. (a) Atom-projected phonon dispersion of I -43d structure exhibiting imaginary modes shown as negative frequencies (ω). Inset: First Brillouin zone (BZ) and high-symmetry paths. (b) Atom-projected phonon dispersion < 10 THz zoomed from (a). Red represents Y, blue for C, and purple for contributions from both as defined in Eq. (2). (c) Formation energy (ΔE_f) with respect to volume (V) for I -43d (220), rhombohedral structure in space group $R3c$ (161), and the low-symmetry structure relaxed from eigenmode 4 in space group $P1$ (1), compared to the experimental data [42] around the equilibrium. (d) Enthalpy difference (ΔH vs p plot computed for the structures with respect to I -43d structure). (e) Primitive unit cell of Y_2C_3 in the $R3c$ and $P1$ structures. For $P1$, the structure is presented along the $[111]$ direction with atomic displacements represented by red arrows according to the imaginary eigenmode 4. (f) Potential energy vs time plot for *ab initio* MD simulations. (g) Zoomed-in sections of the supercell of 320 atoms in the I -43d structure, and (h), (i) those distorted structures having degenerate energy with different C dimer orientations obtained from the MD simulations. The different C dimer orientations due to wobbling motion are highlighted in the dashed red squares.

calculations. Phonon calculations were performed with a momentum transfer grid (\mathbf{q}) of $(2 \times 2 \times 2)$. Further \mathbf{k} mesh and \mathbf{q} mesh were interpolated to $(12 \times 12 \times 12)$ fine mesh to compute the EPC properties. The Coulomb potential μ_c^* was kept fixed at 0.16. The Fermi surfaces were plotted using

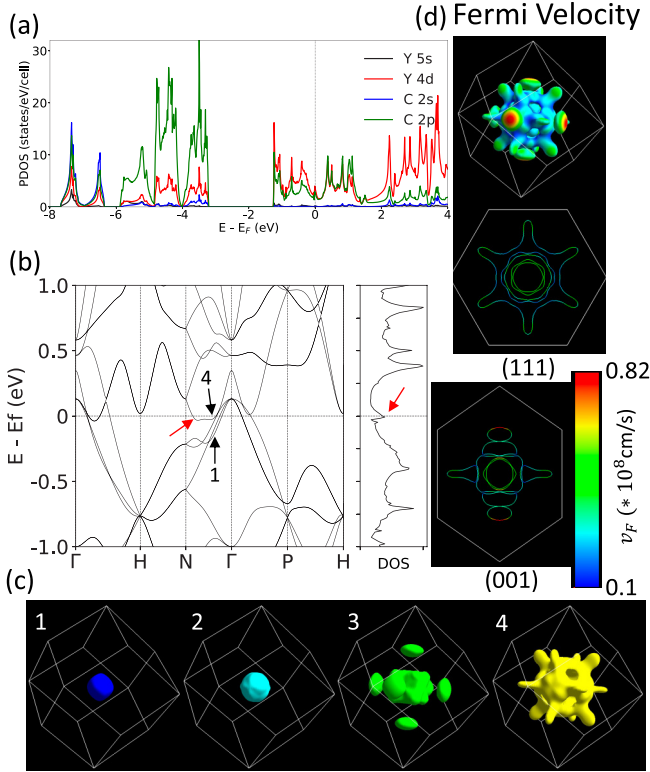


FIG. 3. (a) Projected density of states (PDOS) of Y_2C_3 in the *I*-43d structure on Y 5s, Y 4d, C 2s, and C 2p orbitals, showing a DOS peak near the Fermi level (E_F). (b) Electronic band structure in the range of $E_F \pm 1$ eV showing four bands crossing the E_F (three valence and one conduction bands indicated by the black arrow, indexed from “1” to “4” at the top). The flat band section is along the Γ -N direction (fourth band indicated by the red arrow). (c) Fermi surface (FS) corresponding to the four different bands, labeled by their band index defined in (b). (d) Fermi velocity (v_F) plotted on the FS. Two-dimensional (2D) FS contour on the (111) and (001) planes is also shown.

the FERMISURFER package [34]. The Birch-Murnaghan equations were employed for the calculation of the equation of state (EOS) [35,36]. The formation energy per atom was computed as

$$\Delta E_f = E_{Y_2C_3} - \frac{2}{3}E_Y - \frac{3}{5}E_C, \quad (1)$$

where E_i 's are the total energy per atom of the compound Y_2C_3 and its constituents, namely, Y in a hexagonal-closed-packed and C in the diamond structure. For *ab initio* molecular dynamics (MD) and phase stability calculations with different structural motifs, we used the Vienna *ab initio* simulation package (VASP) [37,38] and projector augmented wave (PAW) method [39] with a kinetic energy cutoff of 500 eV. The MD simulations with NpT ensembles were first performed on the *I*-43d primitive cell of Y_2C_3 to search for new structures at different pressure near and out of the energy minimum of *I*-43d, and then used on the $(2 \times 2 \times 2)$ supercell of the conventional cell with 320 atoms to explore the degeneracy of the C dimer's orientation due to wobbling motion. From the MD trajectories, the snapshots of the low potential energy configurations were selected for full relaxation [40].

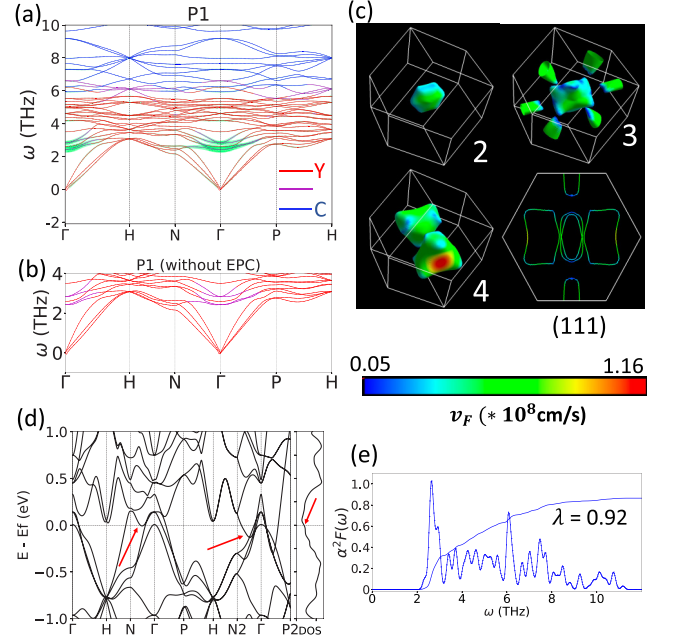


FIG. 4. (a) Atom-projected phonon dispersion for low-symmetry P1 structure of Y_2C_3 relaxed from eigenmode 4. Atom projections are highlighted by red for Y, blue for C, and purple for both contributions. The mode-resolved electron-phonon coupling (EPC) strength (λ) is represented by green. (b) Atom-projected phonon dispersion without the shade of EPC zoomed <4 THz to show the contributions from both Y and C atoms to the λ . (c) Fermi velocity (v_F) plotted over the Fermi surfaces (FS), which are indexed with the same numbers as in Fig. 3, but become distorted because of the relaxation. The 2D FS contour on the (111) plane is also shown. (d) Electronic band structure of the P1 structure showing the absence of flat band, thereby flattening the density of states peak (red arrows) at the Fermi level (E_F). (e) Isotropic Eliashberg spectral function [$\alpha^2F(\omega)$] of P1 structure gives the overall integrated $\lambda = 0.92$.

III. RESULTS AND DISCUSSIONS

In Fig. 1, we first establish that the bcc-type *I*-43d structure is the ground-state phase in the moderate pressure range. (We will use bcc and *I*-43d interchangeably.) In Fig. 1(a), we have plotted the total energy (E) with respect to volume (V) per atom for different phases. First, we have considered all the binary compound structural types containing group-IV elements at the 2:3 composition [Fig. 1(c)] and found several structural motifs of C atoms ($P6_3/mmc$), C trimers ($Pbcn$), zigzag C chains ($Cmcm$), and mixed C dimers and atoms ($Pnma$ and $P-4c2$). Then, we also used *ab initio* MD to explore the energy landscape [40] near and out of the *I*-43d structure at 20 GPa (MD1) and -5 GPa (MD2) for other possible low-symmetry structures [Fig. 1(d)]. We found structures of mixed C dimer and tetramer (MD1-1), mixed C dimer and trimer (MD1-2), and C dimers in a different lattice (MD2-1). As shown by the $E(V)$ EOS in Fig. 1(a), for a large range of volume from 11 to $16 \text{ \AA}^3/\text{atom}$, the *I*-43d structure has the lowest energy, and only for volume larger than the equilibrium of the *I*-43d (negative pressure), two structures ($Pnma$ and MD2-1) become more stable. With the $E(V)$ data, we computed the enthalpies ($H = E + pV$) for different pressure (p) relative to the *I*-43d

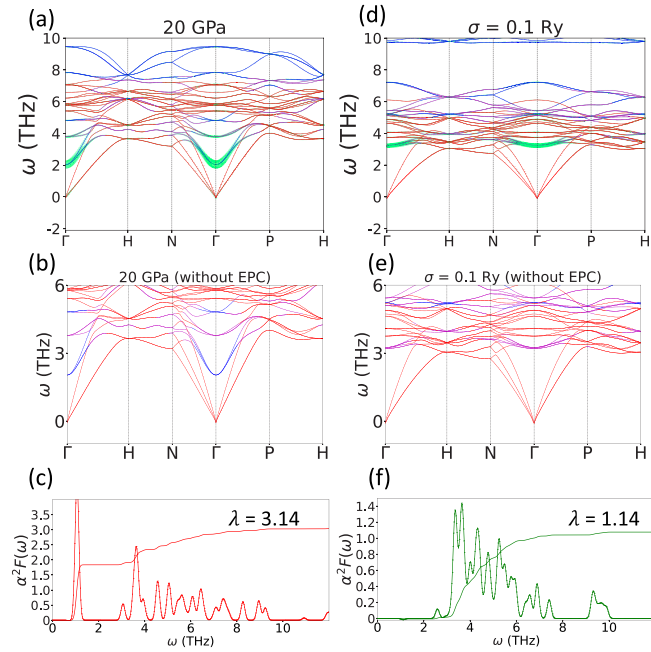


FIG. 5. (a) Atom-projected phonon dispersion of Y_2C_3 in the $I-43d$ structure under 20 GPa. Atom projections are highlighted by red for Y, blue for C, and purple for both contributions. The mode-resolved electron-phonon coupling (EPC) strength (λ) is represented by the green shade. (b) Atom-projected phonon dispersion without the shade of EPC zoomed around the modes with the largest EPC to show the contributions from both Y and C atoms to the λ . (c) Isotropic Eliashberg spectral function [$\alpha^2F(\omega)$] of the $I-43d$ structure under 20 GPa giving the overall $\lambda = 3.14$. [(d)–(f)] Similar plots to [(a)–(c)], with a large electronic smearing of 0.1 Ry at zero pressure. The overall integrated $\lambda = 1.14$. The spectral function [$\alpha^2F(\omega)$] is computed in isotropic Eliashberg approximation and then integrated (dashed lines) for the overall λ .

phase and present in Fig. 1(b). Except for negative pressure of less than -5 GPa (expanding volume), the $I-43d$ phase is preferred up to 40 GPa, which is the range we are focusing on in the current study to stabilize the imaginary phonon modes to reveal their large EPC contribution for enhancing T_c in comparison to the relevant experiments. From the slope of $H(p)$, there are possible structural phase transitions at pressure well above 100 GPa, but it is beyond the scope of the current paper and needs to be further explored in a future work.

Figure 1(c) shows the $I-43d$ structure of Y_2C_3 in the primitive unit cell (20 atoms), where eight Y atoms occupy $16c$ sites and 12 C atoms at $24d$ sites form six dimers. Our PBE-relaxed lattice constant of 8.239\AA and C-C bond length of 1.34\AA agree well with the experimental 8.237\AA and 1.298\AA [41], and also 8.254\AA and 1.33\AA from the previous density functional theory (DFT) calculation [23], respectively. The DFPT-calculated $I-43d$ phonon dispersion is plotted in Fig. 2(a), with the inset showing the Brillouin zone (BZ) and high-symmetry points. To analyze the contribution of different atomic species to phonon eigenmodes, we have summed the atomic displacements of each eigenmode for different species

($|\mathbf{e}_{\nu\mathbf{k}}^i|^2$) as in Eq. (2) and color-coded the dispersion,

$$|\mathbf{e}_{\nu\mathbf{k}}^i|^2 = \sum_{j=1}^{N_i} |\mathbf{e}_{\nu\mathbf{k}}^{ij}|^2, \quad (2)$$

where $\mathbf{e}_{\nu\mathbf{k}}^{ij}$ are the displacements obtained for atom type i from the eigenvector of mode ν for k -point \mathbf{k} by diagonalizing the dynamical matrix, and index j runs to N_i as the number of atoms for type i . For Y_2C_3 in Fig. 2(a), the modes with the highest frequency, ~ 40 THz, are well separated from the rest and solely contributed from the C dimer stretching mode. Our atomic projection also reveals that the modes from 10 to 15 THz are dominated by other C-related motion (blue). In contrast, the Y contributions (red) are mostly around 5 THz due to the much larger mass of Y than C. As zoomed in Fig. 2(b) for the frequency < 10 THz, there are modes with mixed contributions from both Y and C (purple). Interestingly, we find that the three zone-center modes at Γ are imaginary, shown by the negative frequency, and are also dominated by C contributions. Figure 2(e) shows one of the imaginary modes (eigenmode 4) with the arrows representing the direction and size of the atomic displacements for the eigenvector. Usually, the C-related modes are assumed to have high frequency due to the tendency of C to form stronger covalent bonds and smaller mass than Y. But as shown in the Appendix Figs. 6(a)–6(c) with the conventional unit cell, each Y is surrounded by 12 C dimers in a twisted prism, while each C dimer is surrounded by eight Y atoms in a cage of two trapezoids. The wobbling motion of the C dimers within these cages has zero to even negative energy cost, giving rise to the three imaginary optical modes. The other two imaginary modes (eigenmodes 1 and 10) are displayed in Fig. 7 in the Appendix.

The zone-center imaginary phonon modes indicate that the $I-43d$ structure of Y_2C_3 is dynamically unstable. To search for more stable structures, we have used the imaginary modes to distort the primitive unit cell to perform full relaxation with atomic positions and cell vectors, and we find new low-symmetry structures with total energies of 2.34 (modes 4 and 10) and 0.9 meV/atom (mode 1) below that of the $I-43d$ structure. For the most stable structure of mode 4, the lattice symmetry is also the lowest in space group $P1$ (1). We have also considered the cubic to rhombohedral distortion along the $[111]$ direction to retain some symmetry as in space group $R3c$ (161). In Fig. 2(c), the formation energy (ΔE_f) is plotted with respect to V close to the equilibrium for the three structures with gradually lowered symmetry. The ΔE_f of -281 meV/atom agrees well with the experimental -261 meV/atom [42]. The relaxed C-C (Y-C) bond length in the $I-43d$ structure around 1.34 (2.51) \AA is consistent with the previous DFT calculation [23], and also comparable to the experimental 1.298 (2.51) \AA [41]. Compared to the high-symmetry $I-43d$ structure, the $R3c$ and $P1$ structures are more stable at the equilibrium and larger volumes, with $P1$ being the most stable in the lowest symmetry. But at volumes smaller than the equilibrium or under increasing pressure, the three EOS $E(V)$ plots converge to the same curve. In other words, the $I-43d$ structure becomes the ground state under pressure.

In addition to the $E(V)$, we also plot $\Delta H(p)$ in Fig. 2(d), which shows that the low-symmetry bcc-distorted structures

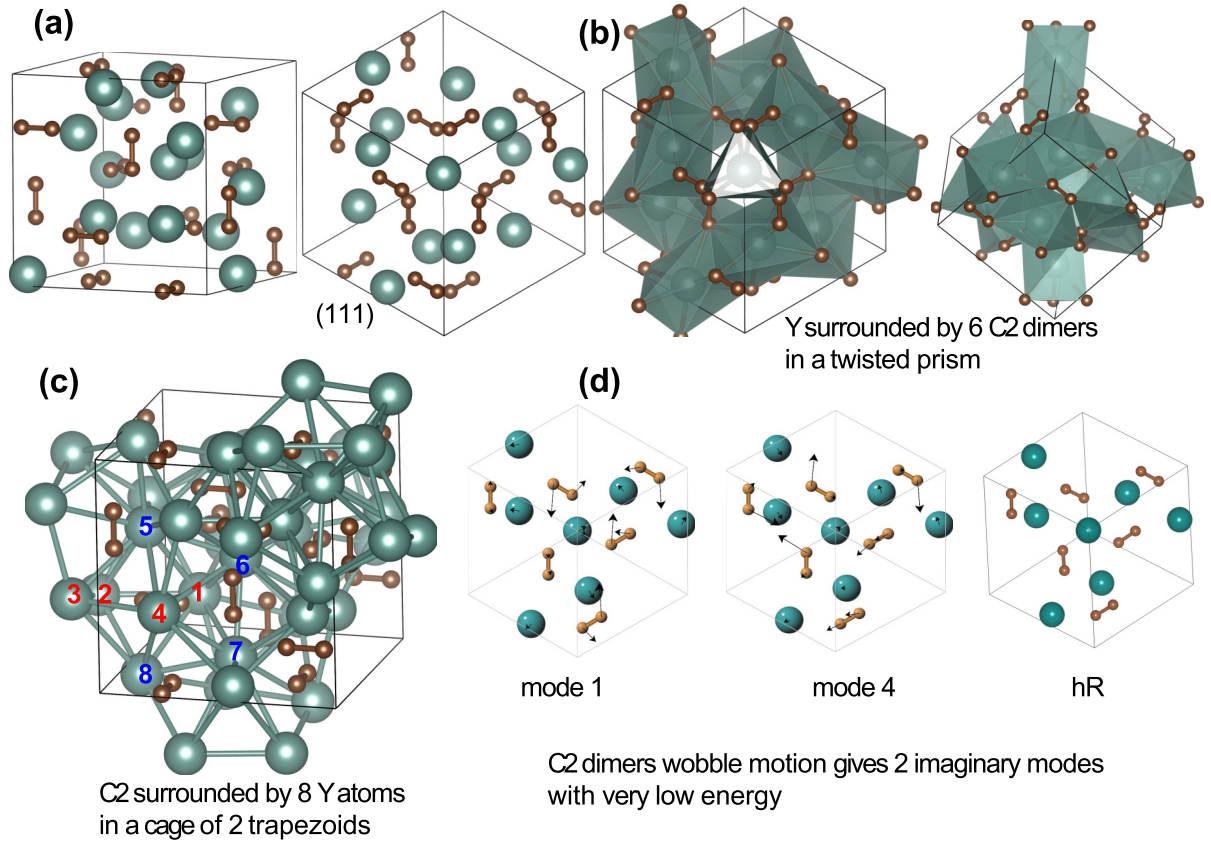


FIG. 6. [(a)–(c)] Conventional body-centered-cubic (bcc) unit cell of Y_2C_3 in space group $I-43d$ (220) viewed from different perspectives as labeled. Y and C atoms are represented by large and small spheres, respectively. (d) Atomic displacements from phonon eigenvectors plotted for mode 1 and mode 4; crystal structure of hR low-symmetry structure in space group $R3c$ (161).

have lower H than the high-symmetry $I-43d$ only in the small pressure range below 7 GPa. However, we would like to point out a major difference between these bcc-distorted structures and the various structures presented in Fig. 1 because, at positive pressure and smaller volume, the EOS of the bcc-distorted structures merges into that of the bcc. The underlying reason is that these distortions are from the wobbling motion of C dimers in the Y cages of $I-43d$, which can have many similarly distorted structures with degenerated energy. Using *ab initio* MD simulation of a supercell of 320 atoms to explore the trajectories of C dimer wobbling motion [Fig. 2(f)], we can then take snapshots of the configurations for full ionic relaxation. For example, we show two configurations with degenerated energy have C dimers in different orientations in Figs. 2(h) and 2(i). Thus, the ensemble of the many bcc-distorted structures with C dimer wobbling motion at finite temperature should still give an overall bcc structure as seen in x-ray diffraction. This type of metastable bcc Y_2C_3 structure is similar to the austenitic NiTi phase, for which the high-symmetry CsCl (B2) structure has imaginary phonon modes and multiple local energy minimums; thus, the overall stable B2 structure is represented by distorted supercells of the B2 structure [43].

To find out the origin of such instability in bcc Y_2C_3 , we have calculated the electronic structures. As plotted in Fig. 3(a), the partial DOS (PDOS) projected on atomic orbitals shows that the bonding states of the C dimer with $2s$

and $2p$ orbitals dominate from -8 to -3 eV, while the Y $4d$ orbitals dominate the empty states above $+2$ eV. In the middle, the hybridization between the C dimer antibonding states and Y $4d$ form a pseudogap from -0.5 to $+0.5$ eV. However, inside this broad pseudogap, there is a sharp local DOS maximum at E_F , which hints at an electronic instability. From the calculated electronic band structures in Fig. 3(b) in the range of ± 1 eV, there are four bands crossing E_F with the corresponding 3D Fermi surface (FS) plotted in Fig. 3(c). As numbered from low to high energy in Figs. 3(b) and 3(c), the first two valence bands form small spherical hole pockets around Γ . The third and highest valence band has disklike features along the Γ - H direction besides a cubic hole pocket. The fourth and lowest conduction band forms spikelike features along the Γ - N direction, besides a spherical double-layered shell around Γ . The spikelike features come from the flat band along the Γ - N direction in Fig. 3(b) and corresponds to the sharp local DOS maximum at -10 meV (red arrow). The Fermi velocity (\mathbf{v}_F), $\nabla_k E_k$, has also been calculated and overlaid on the FS in Fig. 3(d). The maximum value appears on the outer surface of the disklike feature of FS3. 2D cuts of FS along the (111) and (001) planes show the distribution of \mathbf{v}_F with high values across FS1 and FS2, relatively lower value for FS3 except for the disklike feature, and the lowest for FS4 (blue and green patches), consistent with previous result [23]. Although the presence of the flat band in Y_2C_3 has been noted before (Refs. [23,28]), its implication on the

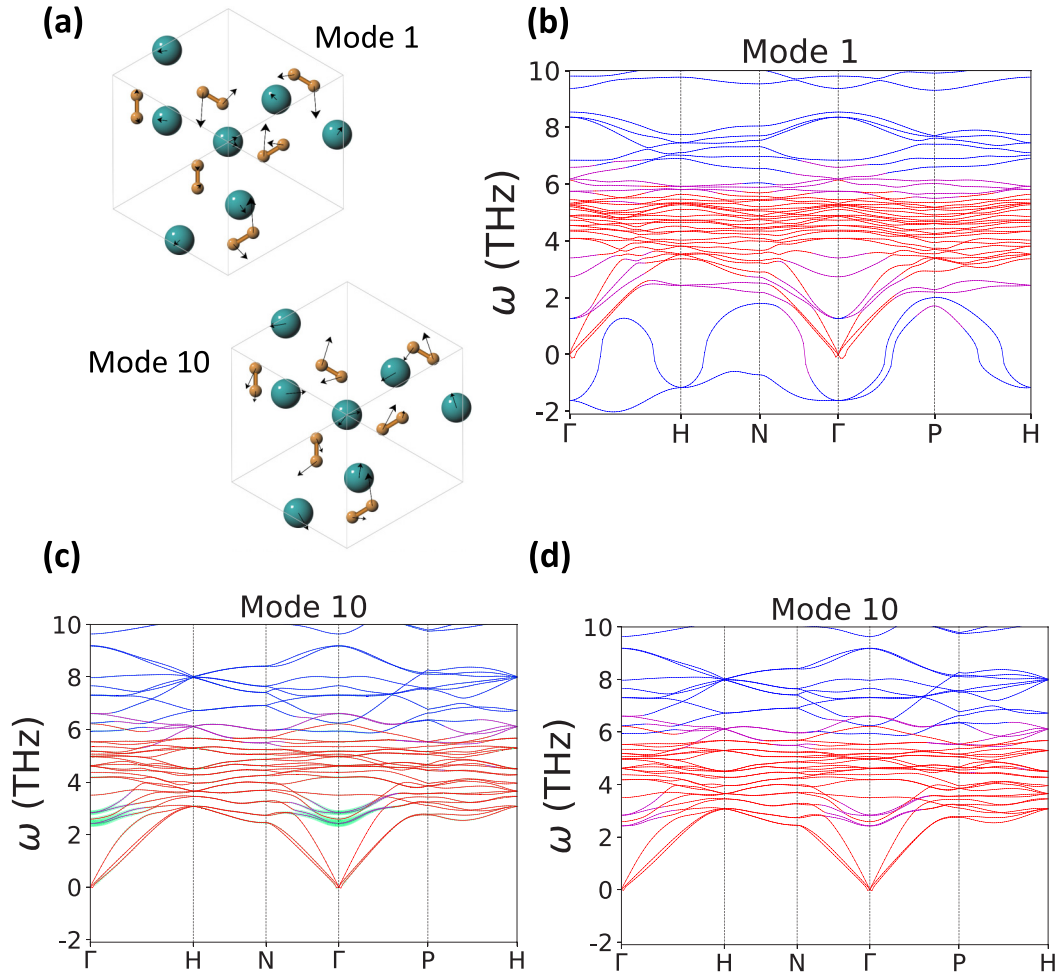


FIG. 7. (a) Eigenmode plotted for modes 1 and 10. (b) Phonon dispersion showing imaginary phonon modes for the distorted lattice from mode 1. (c) Phonon dispersion for the distorted lattice from mode 10 (with same total energy as mode 4) indicating dynamic stability; electron-phonon coupling (EPC) strength is plotted (green color near Γ point close to 2 THz phonon frequency). (d) Same plot as of (c) without EPC, but only with atomic character projection; purple color at the maximum EPC contribution indicates the contribution from both Y (red) and C dimer (blue).

structural instability has only been revealed in our current work by finding the zone-center imaginary phonon modes and the more stable structures via distortion according to the imaginary phonon modes. The flat band in Y_2C_3 is present in the high-symmetry bcc structure, not the low-symmetry bcc-distorted structure at ambient pressure. Figure 8(a) shows the flat band crosses the E_F with increasing pressure in the pressure-stabilized bcc structure. Thus, experimental observation of the flat band in Y_2C_3 requires an angular-resolved photoemission spectroscopy (ARPES) experiment on single-crystal samples of Y_2C_3 at elevated pressure.

After establishing the electronic origin of the instability in bcc Y_2C_3 and finding the more stable low-symmetry $P1$ structure, next we calculate EPC in DFPT to explain SC properties. In Fig. 4, we plot the phonon dispersion of the $P1$ structure relaxed from eigenmode 4 (~ 2.34 meV/atom more stable than $I-43d$) with [Fig. 4(a)] and without [Fig. 4(b)] the mode-resolved EPC projections. Atomic characters are also similarly projected as in Figs. 2(d) and 2(e). Due to the lowest symmetry, much degeneracy at the high-symmetry points has been lifted in $P1$ [Fig. 4(a)] when compared to the $I-43d$

phonon dispersion [Fig. 2(e)]. Importantly, the $P1$ structure does not have imaginary modes and is dynamically stable. The original imaginary modes in $I-43d$ are now stabilized in the low-frequency range of 2–3 THz at Γ . Moreover, the largest EPC contribution is found around Γ (green shade) along the Γ - H , Γ - N , and Γ - P directions within the same low-frequency range, where both C dimers and Y atoms provide significant contributions [see purple in Fig. 4(b) without EPC]. As confirmed in the Eliashberg spectral function of Fig. 4(e), the largest EPC contribution peak comes from the 2–3 THz range, followed by another peak around 6 THz, in which both have the mixed C and Y characters, giving an overall EPC strength λ of 0.92, logarithmic average of phonon frequencies (ω_{\log}) of 219.6 K, and T_c of 9.3 K, as listed in Table I. The calculated T_c is in good agreement with the experimental data. For the change in electronic structures, the FS of the $P1$ structure now consists of only three bands, completely removing the spikelike features due to the flat band along the Γ - N direction [Fig. 4(b)]. As a result, the electronic instability associated with the flat band is eliminated, and the local DOS maximum at E_F is flattened out, as seen in Fig. 4(c) (red arrows). The

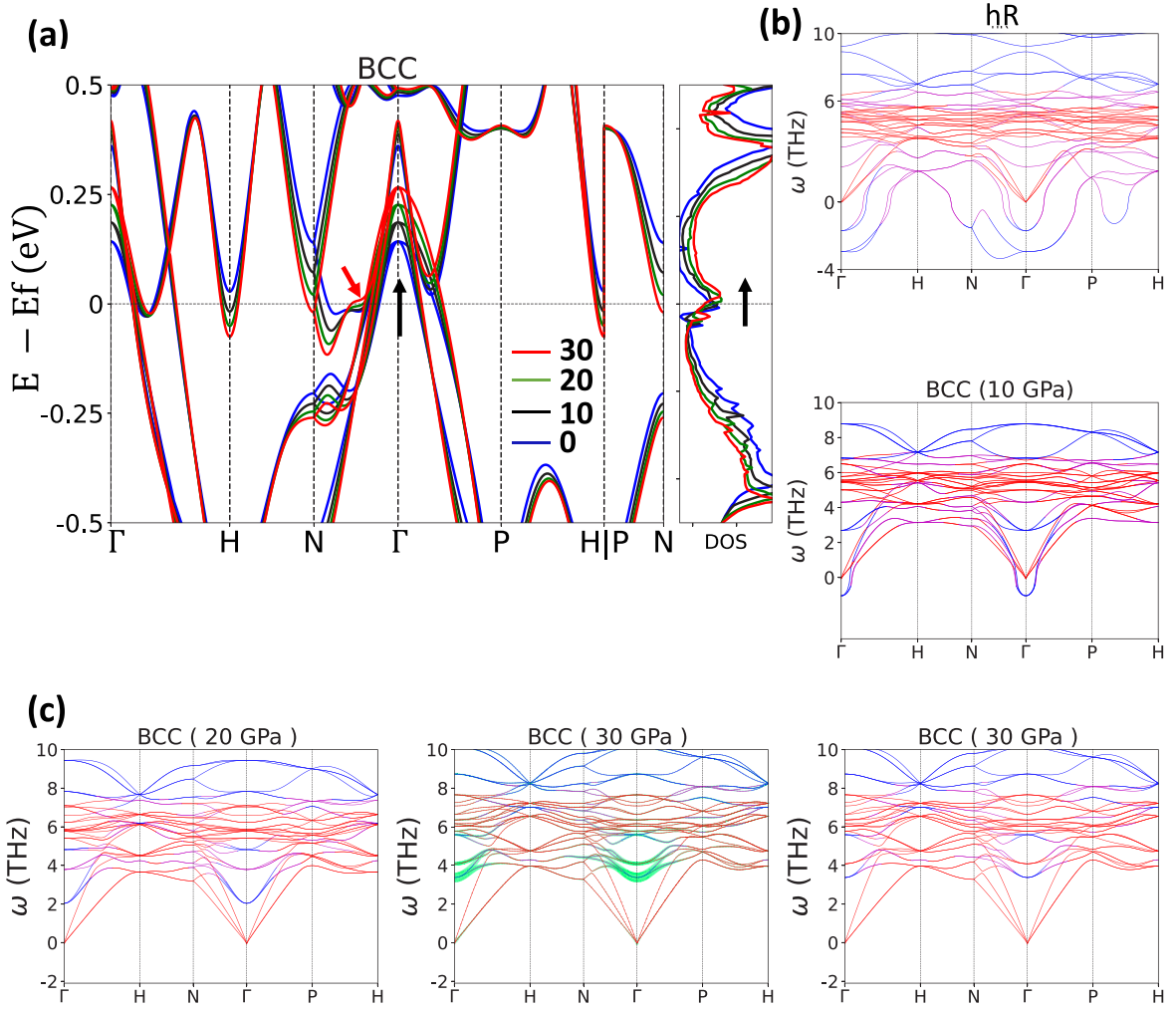


FIG. 8. (a) Shifting of local density of states (DOS) maximum towards higher-energy region with increasing pressure (from 0 to 30 GPa), leaving relatively smooth DOS at E_F (black arrow on right plot). A section of flat band near E_F (shown by red arrow) is also pushed towards the conduction band region (black arrow on left plot). (b) Phonon dispersion presenting dynamic instability of low-symmetry $R3c$ structure and $I-43d$ (BCC) under 10 GPa pressure. (c) Phonon dispersion plots with projected atomic character for various pressure with/without EPC; two soft modes stabilized at 20 GPa are pushed upward with 30 GPa pressure.

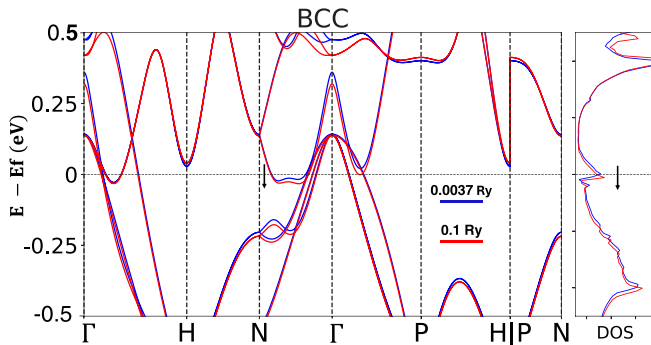


FIG. 9. Shifting of flat band along the Γ -N and local density of states (DOS) maximum away from the E_F towards lower energy with increased Gaussian smearing from 0.0037 to 0.1 Ry. Note that the DOS calculation is performed with the tetrahedron method, after the charge density is converged self-consistently with different smearing values.

results from the other $I-43d$ imaginary phonon modes, namely, modes 1 (~ 0.9 meV/atom lower) and 10 (~ 2.34 meV/atom lower, similar to eigenmode 4), are presented in Fig. 7. The corresponding properties are listed in Table I showing a similar T_c to the $P1$ structure of eigenmode 4. Thus, one of the key findings of our work is that the EPC for the phonon-mediated SC in Y_2C_3 with a sizable T_c arise from the stabilized imaginary phonon modes after removing the flat band and electronic instability, and the largest EPC contributions are from these stabilized low-energy optical phonon modes of mixed C and Y characters.

Besides distorting the $I-43d$ structure for more stable low-symmetry structures, increasing pressure and electronic smearing are other ways to shift the flat band away from E_F (see Figs. 8 and 9) to stabilize the imaginary phonon modes. As plotted in Fig. 5(d), a large electronic smearing of 0.1 Ry on the $I-43d$ structure reasonably mimics the results of the low-symmetry $P1$ structure, as seen in the phonon dispersion of Fig. 5(e) and spectral function $[\alpha^2F(\omega)]$ of Fig. 5(f).

TABLE I. EPC strength λ , logarithmic average of phonon frequencies ω_{\log} , and critical temperature T_c computed from isotropic Eliashberg approximation with distorted structures, pressure, and large electronic smearing for Y_2C_3 using the Coulomb potential μ_c^* of 0.16. (These quantities are not available for the dynamically unstable structures with imaginary modes, for example, $\text{Y}_2\text{C}_3 < 20$ GPa, $\sigma < 0.10$ Ry, and distorted structure with mode 1.) Experimental T_c for Y_2C_3 ranges from 6 to 18 K, depending on synthesis conditions and measurement techniques [16,17].

| Stabilization | λ | ω_{\log} (K) | T_c (K) |
|--------------------|-----------|---------------------|-----------|
| Mode 4 | 0.92 | 219.6 | 9.3 |
| Mode 10 | 0.93 | 219.4 | 9.5 |
| 20 GPa | 3.14 | 96.1 | 16.0 |
| 30 GPa | 1.38 | 263.6 | 22.3 |
| $\sigma = 0.10$ Ry | 1.14 | 228.5 | 14.5 |

But pressure stabilizes these imaginary phonon modes with additionally interesting behaviors. As shown in Figs. 5(a) and 8(c), the pressure of 20 GPa stabilizes the imaginary phonon modes, one at ~ 4 THz and the other at as low as ~ 2 THz, with unusually large λ coming from those modes with large contribution from C dimers. The increasing pressure also shifts the flat band and the associated local DOS maximum peak first to cross E_F and then to higher energy away from E_F , resulting in a smooth part of DOS at E_F , thereby stabilizing the imaginary phonon modes Fig. 8(a). As listed in Table I, the large $\lambda \sim 3.14$ at 20 GPa and low $\omega_{\log} \sim 96.1$ K are the results of the extremely soft or low-energy modes with a large EPC contribution, also seen in Fig. 5(c). For a further increase of pressure to 30 GPa, the lowest soft mode is pushed upward to bring the two stabilized phonon modes close to each other at Γ , similar to the cases of the $P1$ structure and the large electronic smearing, but achieving both a larger λ of 1.38 and a larger ω_{\log} of 263.6 K [Fig. 8(c)], thereby enhancing the T_c from 9.3 and 14.5 K to 22.3 K. This trend of higher T_c for smaller lattice constants under pressure is consistent with the experimental observation [16,17], where an increase of T_c from sub-10 K to 18 K has been observed when the lattice constant is decreased from 8.24 to 8.20 Å, mostly due to different heat treatment and sintering conditions.

IV. CONCLUSIONS

In conclusion, we find that the high-symmetry body-centered-cubic (bcc) $I-43d$ structure of Y_2C_3 is dynamically unstable with zone-center imaginary optical phonon modes from C dimer wobbling motion due to the electronic instability from a flat band at the Fermi level (E_F). Once the imaginary modes are stabilized in a more stable low-symmetry structure, under pressure or with a large electronic smearing, these low-energy modes of mixed C and Y characters give rise to strong electron-phonon coupling (EPC) strength determining the superconducting properties. Our work demonstrates the necessity of further exploration in the compounds with imaginary phonon modes. EPC calculations may not always be feasible for the distorted structures due

to low symmetry for large unit cells; however, pressure and electronic smearing are the alternatives to stabilize the imaginary phonon modes to study superconductivity. This can open a myriad of opportunities to discover high-temperature superconductors via high-throughput screening. Furthermore, we provide a thorough analysis of the phase stability of Y_2C_3 . We have considered the different structural motifs of binary compounds containing group-IV elements at the 2:3 composition and also explored energy landscapes via *ab initio* molecular dynamics near and out of the bcc structure. We plot their enthalpy vs pressure to confirm that the bcc-type structures with C dimers are indeed preferred in the low to medium pressure range. Because of the wobbling motion of the C dimers, there are many local energy minimums of the bcc-distorted structures with degenerated energies. Consequently, the ensemble average of numerous bcc-distorted structures with C dimer wobbling motion at finite temperature is expected to yield an overall bcc structure, consistent with what was observed in x-ray diffraction.

ACKNOWLEDGMENTS

We acknowledge Dr. Lorenzo Paulatto for the helpful discussion of atom-projected phonon dispersion. This work was supported by Ames National Laboratory LDRD and U.S. Department of Energy, Office of Basic Energy Science, Division of Materials Sciences and Engineering. Ames National Laboratory is operated for the U.S. Department of Energy by Iowa State University under Contract No. DE-AC02-07CH11358.

APPENDIX

Figure 6 illustrates the different views of the Y_2C_3 crystal. In the high-symmetry body-centered-cubic (bcc) structure in space group $I-43d$ (220), each Y ion is enclosed by six C dimers arranged in a twisted prism configuration. Conversely, each C dimer is surrounded by eight Y atoms forming a cage comprised of two trapezoids. This arrangement results in a wobbling motion of the C dimer, contributing to its inherent instability. In Fig. 7, phonon dispersion plots are presented for different structures of lattice distortion from different imaginary phonon modes, including mode 10 (which exhibits the same total energy as mode 4 mentioned in the main text) and mode 1 (slightly higher in total energy). Figure 8 shows the influence of pressure on the electronic band structure and dynamic stability. Upon applying pressure exceeding 20 GPa, the flat band in close proximity to the Fermi level (E_F) undergoes an upward shift. This change causes the local maximum of the density of states (DOS) to shift towards the conduction band region, leaving behind a relatively smoother region at E_F . As a result, the electronic instability is gradually removed and the imaginary phonon modes become stabilized, which provides significant electron-phonon coupling (EPC). Finally, Fig. 9 illustrates the shift of the flat band and local DOS peak away from the E_F resulting from increased electronic smearing. After charge density is converged self-consistently with different smearing values, the DOS calculation is then performed with the tetrahedron method.

- [1] Y. Li, J. Hao, H. Liu, Y. Li, and Y. Ma, The metallization and superconductivity of dense hydrogen sulfide, *J. Chem. Phys.* **140**, 174712 (2014).
- [2] G. Webb, F. Marsiglio, and J. Hirsch, Superconductivity in the elements, alloys and simple compounds, *Physica C: Supercond. Appl.* **514**, 17 (2015).
- [3] A. P. Drozdov, M. I. Erements, I. A. Troyan, V. Ksenofontov, and S. I. Shylin, Conventional superconductivity at 203 kelvin at high pressures in the sulfur hydride system, *Nature (London)* **525**, 73 (2015).
- [4] W. E. Pickett, Colloquium: Room temperature superconductivity: The roles of theory and materials design, *Rev. Mod. Phys.* **95**, 021001 (2023).
- [5] B. Lilia, R. Hennig, P. Hirschfeld, G. Profeta, A. Sanna, E. Zurek, W. E. Pickett, M. Amsler, R. Dias, M. I. Erements *et al.*, The 2021 room-temperature superconductivity roadmap, *J. Phys.: Condens. Matter* **34**, 183002 (2022).
- [6] K. Choudhary and K. Garrity, Designing high- T_c superconductors with BCS-inspired screening, density functional theory, and deep-learning, *npj Comput. Mater.* **8**, 244 (2022).
- [7] S. Baroni, S. De Gironcoli, A. Dal Corso, and P. Giannozzi, Phonons and related crystal properties from density-functional perturbation theory, *Rev. Mod. Phys.* **73**, 515 (2001).
- [8] A. Dal Corso, Density-functional perturbation theory with ultrasoft pseudopotentials, *Phys. Rev. B* **64**, 235118 (2001).
- [9] A. Migdal, Interaction between electrons and lattice vibrations in a normal metal, *Sov. Phys. JETP* **7**, 996 (1958).
- [10] G. Eliashberg, Interactions between electrons and lattice vibrations in a superconductor, *Sov. Phys. JETP* **11**, 696 (1960).
- [11] P. B. Allen, Neutron spectroscopy of superconductors, *Phys. Rev. B* **6**, 2577 (1972).
- [12] P. B. Allen and R. Dynes, Transition temperature of strong-coupled superconductors reanalyzed, *Phys. Rev. B* **12**, 905 (1975).
- [13] E. R. Margine and F. Giustino, Anisotropic Migdal-Eliashberg theory using Wannier functions, *Phys. Rev. B* **87**, 024505 (2013).
- [14] R. Cava, H. Takagi, H. Eisaki, H. Zandbergen, T. Siegrist, B. Batlogg, J. Krajewski, W. Peck Jr, S. Carter, K. Mizuhashi *et al.*, Good news from an abandoned gold mine: A new family of quaternary intermetallic superconductors, *Physica C: Supercond.* **235-240**, 154 (1994).
- [15] Y. Sun, I. Rusakova, R. Meng, Y. Cao, P. Gautier-Picard, and C. Chu, The 23 K superconducting phase YPd_2B_2C , *Physica C: Supercond.* **230**, 435 (1994).
- [16] M. C. Krupka, A. L. Giorgi, N. H. Krikorian, and E. G. Szklarz, High pressure synthesis and superconducting properties of yttrium sesquicarbide, *J. Less-Common Met.* **17**, 91 (1969).
- [17] G. Amano, S. Akutagawa, T. Muranaka, Y. Zenitani, and J. Akimitsu, Superconductivity at 18 K in yttrium sesquicarbide system, Y_2C_3 , *J. Phys. Soc. Jpn.* **73**, 530 (2004).
- [18] K. Sugawara, T. Sato, S. Souma, T. Takahashi, and A. Ochiai, Anomalous superconducting-gap symmetry of noncentrosymmetric La_2C_3 observed by ultrahigh-resolution photoemission spectroscopy, *Phys. Rev. B* **76**, 132512 (2007).
- [19] S. Kuroiwa, Y. Saura, J. Akimitsu, M. Hiraishi, M. Miyazaki, K. H. Satoh, S. Takeshita, and R. Kadono, Multigap superconductivity in sesquicarbides La_2C_3 and Y_2C_3 , *Phys. Rev. Lett.* **100**, 097002 (2008).
- [20] J. Chen, M. B. Salamon, S. Akutagawa, J. Akimitsu, J. Singleton, J. L. Zhang, L. Jiao, and H. Q. Yuan, Evidence of nodal gap structure in the noncentrosymmetric superconductor Y_2C_3 , *Phys. Rev. B* **83**, 144529 (2011).
- [21] S. Akutagawa, T. Ohashi, H. Kitano, A. Maeda, J. Goryo, H. Matsukawa, and J. Akimitsu, Quasiparticle electronic structure of a new superconductor, Y_2C_3 , in the mixed state investigated by specific heat and flux-flow resistivity, *J. Phys. Soc. Jpn.* **77**, 064701 (2008).
- [22] M. Krupka, A. Giorgi, N. Krikorian, and E. Szklarz, High-pressure synthesis of yttrium-thorium sesquicarbide: A new high-temperature superconductor, *J. Less-Common Met.* **19**, 113 (1969).
- [23] Y. Nishikayama, T. Shishidou, and T. Oguchi, Electronic properties of Y_2C_3 by first-principles calculations, *J. Phys. Soc. Jpn.* **76**, 064714 (2007).
- [24] I. Shein and A. Ivanovskii, Electronic properties of the novel 18-K superconducting Y_2C_3 as compared with 4-K YC_2 from first principles calculations, *Solid State Commun.* **131**, 223 (2004).
- [25] D. J. Singh and I. I. Mazin, Electronic structure and electron-phonon coupling in the 18 K superconductor Y_2C_3 , *Phys. Rev. B* **70**, 052504 (2004).
- [26] L. Jin, Y. Liu, X. Zhang, X. Dai, and G. Liu, Sixfold, fourfold, and threefold excitations in the rare-earth metal carbide R_2C_3 , *Phys. Rev. B* **104**, 045111 (2021).
- [27] J. S. Kim, W. Xie, R. K. Kremer, V. Babizhetskyy, O. Jepsen, A. Simon, K. S. Ahn, B. Raquet, H. Rakoto, J.-M. Broto, and B. Ouladdiaf, Strong electron-phonon coupling in the rare-earth carbide superconductor La_2C_3 , *Phys. Rev. B* **76**, 014516 (2007).
- [28] W. E. Pickett, The next breakthrough in phonon-mediated superconductivity, *Physica C Supercond.* **468**, 126 (2008).
- [29] P. Giannozzi, S. Baroni, N. Bonini, M. Calandra, R. Car, C. Cavazzoni, D. Ceresoli, G. L. Chiarotti, M. Cococcioni, I. Dabo *et al.*, QUANTUM ESPRESSO: A modular and open-source software project for quantum simulations of materials, *J. Phys.: Condens. Matter* **21**, 395502 (2009).
- [30] P. Giannozzi, O. Andreussi, T. Brumme, O. Bunau, M. B. Nardelli, M. Calandra, R. Car, C. Cavazzoni, D. Ceresoli, M. Cococcioni *et al.*, Advanced capabilities for materials modelling with QUANTUM ESPRESSO, *J. Phys.: Condens. Matter* **29**, 465901 (2017).
- [31] G. Prandini, A. Marrazzo, I. E. Castelli, N. Mounet, and N. Marzari, Precision and efficiency in solid-state pseudopotential calculations, *npj Comput. Mater.* **4**, 72 (2018).
- [32] K. F. Garrity, J. W. Bennett, K. M. Rabe, and D. Vanderbilt, Pseudopotentials for high-throughput DFT calculations, *Comput. Mater. Sci.* **81**, 446 (2014).
- [33] J. P. Perdew, K. Burke, and M. Ernzerhof, Generalized gradient approximation made simple, *Phys. Rev. Lett.* **77**, 3865 (1996).
- [34] M. Kawamura, Fermisurfer: Fermi-surface viewer providing multiple representation schemes, *Comput. Phys. Commun.* **239**, 197 (2019).
- [35] F. D. Murnaghan, The compressibility of media under extreme pressures, *Proc. Natl. Acad. Sci. USA* **30**, 244 (1944).
- [36] F. Birch, Finite elastic strain of cubic crystals, *Phys. Rev.* **71**, 809 (1947).
- [37] G. Kresse and J. Furthmüller, Efficiency of *ab initio* total energy calculations for metals and semiconductors using a plane-wave basis set, *Comput. Mater. Sci.* **6**, 15 (1996).

- [38] G. Kresse and J. Furthmüller, Efficient iterative schemes for *ab initio* total-energy calculations using a plane-wave basis set, *Phys. Rev. B* **54**, 11169 (1996).
- [39] P. E. Blöchl, Projector augmented-wave method, *Phys. Rev. B* **50**, 17953 (1994).
- [40] L.-L. Wang and D. D. Johnson, Density functional study of structural trends for late-transition-metal 13-atom clusters, *Phys. Rev. B* **75**, 235405 (2007).
- [41] T. Mochiku, T. Nakane, H. Kito, H. Takeya, S. Harjo, T. Ishigaki, T. Kamiyama, T. Wada, and K. Hirata, Crystal structure of yttrium sesquicarbide, *Physica C: Superconduct.* **426-431**, 421 (2005).
- [42] V. Novokshonov, Synthesis of sesquicarbides of heavy rare earths and yttrium at high pressures and temperatures, *Zhurnal Neorganicheskoy Khimii* **25**, 684 (1980).
- [43] N. A. Zarkevich and D. D. Johnson, Stable atomic structure of NiTi austenite, *Phys. Rev. B* **90**, 060102(R) (2014).